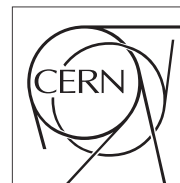


The Compact Muon Solenoid Experiment

Analysis Note

The content of this note is intended for CMS internal use and distribution only



March 5, 2009

Draft Version

QCD studies in CMS with Multijets at $\sqrt{s} = 10$ TeV.

S. Bose

Tata Institute of Fundamental Research, India

S. Banerjee

Fermi National Accelerator Laboratory, Batavia, IL, USA

N. Varelas

University of Illinois at Chicago, Chicago, IL, USA

Abstract

The prospects of QCD studies with multi-jet events at the CMS experiment at the Large Hadron Collider are presented in this note. The analysis targets the first 10 pb^{-1} of proton-proton collisions at $\sqrt{s} = 10$ TeV. Various multijet kinematic and angular distributions are studied. Systematic effects due to detector corrections and usage of different jet algorithms are looked into. Major sources of systematic uncertainties for some of the variables are estimated. Comparisons are made between the predictions from the leading order calculations inside the PYTHIA event generator and matrix element generators. The normalized multijet distributions are found to be robust under variations of the jet energy scale and resolution effects, which make them suitable for early data analysis and tuning of Monte Carlo models.

Contents

1	Introduction	3
2	Definition	4
2.1	3-parton variables	4
2.2	4-parton variables	5
3	Monte Carlo Sample and Event Selection	6
4	Trigger selection	7
5	Multi-jet topological distributions	7
5.1	Topologies of Three-Jet events	8
5.2	Topologies of Four-Jet events	9
6	Sensitivity study	10
6.1	Sensitivity to jet clustering algorithms	10
6.2	Sensitivity due to jet energy corrections	11
7	Detector Effects	11
7.1	Energy resolution	11
7.2	Position resolution	11
7.2.1	Resolution in Eta	11
7.2.2	Resolution in Phi	13
7.3	Combined effect	13
8	Systematic uncertainty	13
8.1	Jet Energy Scale	13
8.2	Systematic uncertainty due to trigger bias	13
8.3	Systematic uncertainty due to event selection	14
9	Comparison to matrix element calculations	14
9.1	ALPGEN production	15
9.2	Comparison to ALPGEN	15
10	Conclusions	16

1 Introduction

In proton-proton collisions, interactions take place between the partons of the colliding protons. Due to the high center-of-mass energy available, the partonic interactions can be in good approximation considered as $2 \rightarrow 2$ scattering processes. In the cases where the scattering is hard (large momentum transfer), the scattered partons will hadronize into highly collimated bunches of particles that will be measured in the calorimeter as high transverse momentum jets. The study of the high p_T jets is twofold: test the QCD predictions and look for physics beyond the Standard Model. Since the parton scattering is practically an elementary QCD process, the jet distributions can be calculated from first principles, provided that reasonable hadronization modeling is available. Therefore, the high p_T jets serve as a direct test of perturbative QCD (pQCD). Also, their production is sensitive to the strong coupling constant α_S and precise knowledge of the jet cross section can help reduce the uncertainties of the parton distribution functions (PDFs) of the proton. High p_T jets are furthermore sensitive to new Physics (e.g quark compositeness, resonances) and given the high reach in p_T at LHC current limits can be improved and discoveries are possible even at startup.

Jet production is the dominant process in high p_T hadron-hadron collisions. This process is well described by perturbative QCD in terms of a point-like scattering cross sections convoluted with a pair of parton distribution functions that express the momentum distribution of partons within the proton. The hard-scattering cross section itself can be written as an expansion in the strong coupling constant $\alpha_s(Q^2)$. The leading term in this expansion corresponds to the emission of two partons. The next term includes diagrams where an additional parton is observed in the final state due to hard gluon radiation (e.g. $gg \rightarrow ggg$). Such diagrams, examples of which are seen in Figure 1, diverge when any of the three partons become soft or when two of the partons become collinear.

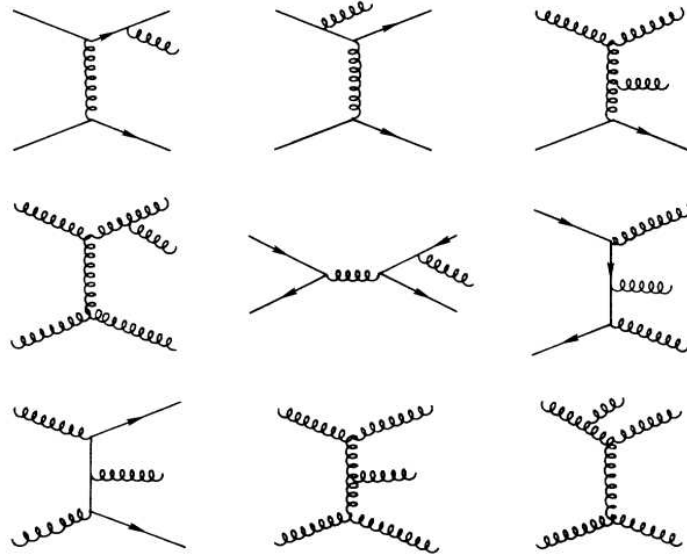


Figure 1: Feynman diagrams for 3 parton final state in hadron collisions.

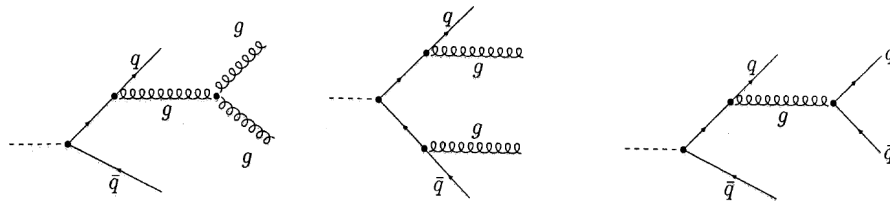


Figure 2: Feynman diagrams for 4-parton final state.

Perturbative QCD predicts two classes of 4-jet events which correspond to the processes: $q\bar{q}/gg \rightarrow q\bar{q}gg$ and $q\bar{q}/gg \rightarrow q\bar{q}q\bar{q}$. The first diagram in the Figure2 contains a *three gluon vertex*, a consequence of the non-Abelian nature of QCD.

In order to study the three and four parton final state we define a class of observables for QCD studies. They have

been studied widely in earlier LEP (e^+e^-) and Tevatron ($p\bar{p}$) experiments. In this note we present a study of the multi-jet observables based on simulation samples of hadronic events with the CMS detector. We compute the kinematic and angular properties of these variables from the four-vectors of jets.

The goal of this study is to show the expected sensitivity of these observables to the choice of the jet algorithm, as well as to the effect of jet energy corrections. We study the detector effect by smearing the jet energy and position resolution. We try to present a first estimate of the expected dominant systematic uncertainty at start up data taking, resulting from limited knowledge of the jet energy scale and event selection. Finally we show the sensitivity of the chosen observables to distinguishing models of QCD multi-jet production.

2 Definition

2.1 3-parton variables

The topological variables used in this note are defined in the parton or jet centre-of-mass system (CM). The topological properties of the three-parton final state in the centre-of-mass system can be described in terms of six variables [1]. Three of the variables reflect partition of the CM energy among the three final-state partons. The other three variables define the spatial orientation of the planes containing the three partons.

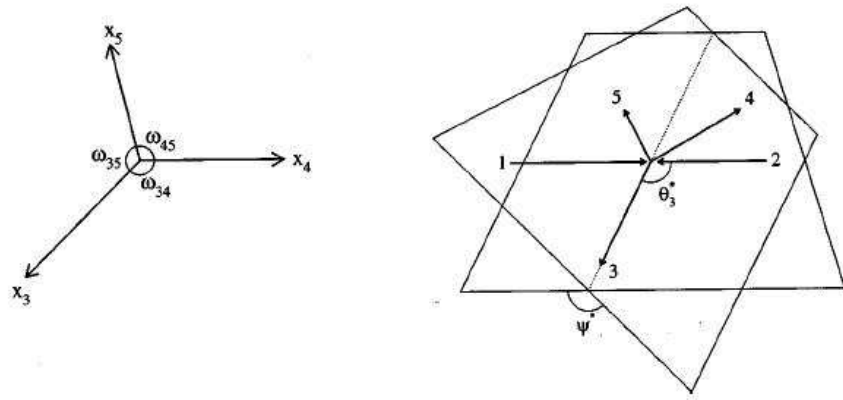


Figure 3: An Illustration of the three-jet angular variables - ψ^* and θ_3^* . The angle ψ^* is the angle between the plane containing the beam line and the highest-energy jet in the CM frame of the 3-jet system, and the next two highest-energy jets. As $\psi^* \rightarrow 0^\circ$ or 180° , the contribution of initial-state radiation from incoming partons increase the rate.

It is convenient to introduce the notation $1+2 \rightarrow 3+4+5$ for the three-parton process. Here, numbers 1 and 2 refer to incoming partons while the numbers 3, 4, and 5 label the outgoing partons, ordered in descending CM energies, i.e., $E_3 > E_4 > E_5$. The final state parton energy is an obvious choice for the topological variables for the three-parton final state. For simplicity, E_i ($i = 3, 4, 5$) is often replaced by the scaled variable x_i ($i = 3, 4, 5$), which is defined by $x_i = 2E/\sqrt{\hat{s}}$, where \hat{s} is the centre-of-mass energy of the hard scattering process. By definition, $x_3 + x_4 + x_5 = 2$. For massless jets the scaled parton energies x_i and the angles between partons (ω_{jk} , with $j, k = 3, 4, 5$) for the three parton final state have the relationship:

$$x_i = \frac{2 \sin \omega_{jk}}{\sin \omega_{34} + \sin \omega_{45} + \sin \omega_{53}}$$

where $i, j, k = 3, 4, 5$ and $i \neq j \neq k$. Clearly, the internal structure of the three-parton final state is completely determined by any two scaled parton energies. The angles that fix the event orientation can be chosen to be (1) the cosine Of the polar angle with respect to the beam ($\cos \theta_3^*$) of parton 3, (2) the azimuthal angle of parton 3 (ϕ_3), and (3) the angle between the plane containing partons 1 and 3 and the plane containing partons 4 and 5 (ψ^*) defined by

$$\cos \psi^* = \frac{(\vec{p}_1 \times \vec{p}_3) \cdot (\vec{p}_4 \times \vec{p}_5)}{|\vec{p}_1 \times \vec{p}_3| |\vec{p}_4 \times \vec{p}_5|}$$

where \vec{p}_i is the parton momentum. Figure 3 illustrates the definition of the topological variables for the three-parton final state. Singularities for configurations where two outgoing partons are collinear result in an increased prob-

ability of unequal energy sharing between jets. Divergences resulting from an outgoing parton which is collinear with the beam direction cause structure in the angle between the plane containing the three-jet momenta and the plane containing the beam the beam line and the leading jet, ψ^* (Figure 3). For a dijet process the angle between the planes would be 90 degrees. For unpolarized beams (as at the LHC), the ϕ_3^* distribution is uniform. Therefore, only four independent kinematic variables are needed to describe the topological properties of the three-parton final state. In this note, they are chosen to be x_3 , x_5 , $\cos \theta_3^*$, and ψ^* .

Another set of interesting variables is the scaled invariant mass of jet pairs:

$$\mu_{ij} = \frac{m_{ij}}{\sqrt{s}} \equiv \sqrt{x_i x_j (1 - \cos \omega_{ij})/2}, \quad i, j = 3, 4, 5 \quad \text{and} \quad i \neq j$$

where m_{ij} is the invariant mass of partons i and j and ω_{ij} is the opening angle between the two partons. The scaled invariant mass (μ_{ij}) is sensitive to the scaled energies of the two partons, the angle between the two partons, and the correlations between these variables. Using dimensionless variables and making comparisons of normalized distributions minimizes the systematic uncertainties due to detector resolution and jet energy scale and therefore facilitates comparison between data and theoretical calculation.

Another set of variable, namely, the Ellis-Karliner angle λ [2] between the third and first jet, defined in the centre of mass system of jets 2 and 3, allows a clear distinction between spin-1 and spin-0 gluons. For massless partons:

$$|\cos \lambda| = \frac{x_2 - x_3}{x_1}$$

2.2 4-parton variables

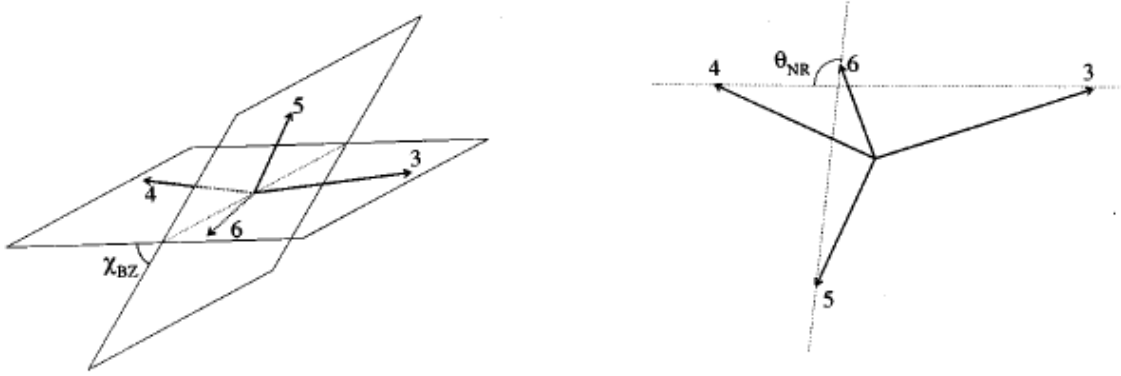


Figure 4: Illustration of the Bengtson-Zerwas angle (χ_{BZ}) and the Nachtmann-Reiter angle (θ_{NR}) definitions for the four jet events. The left cartoon shows the Bengtson-Zerwas angle which is the angle between the plane containing the two leading jets and the plane containing the two non-leading jets. The right cartoon shows the Nachtmann-Reiter angle which is the angle between the momentum vector differences of the two leading jets and the two non-leading jets.

The four-parton final state is more complicated. Apart from the CM energy, eight independent parameters are needed to completely define a four-parton final state in its centre-of-mass system. Two of these define the overall event orientation while the other six fix the internal structure of the four-parton system. In contrast to the three-parton final state, there is no simple relationship between the scaled parton energies and the opening angles between partons. Consequently, the choice of topological variables is less obvious in this case. Variables are defined here in a way similar to those investigated for the three-parton final state. The four partons are ordered in descending CM energy and labeled from 3 to 6. The variables include the scaled energies (x_i , with $i = 3, \dots, 6$), the cosines of polar angles ($\cos \theta_i^*$, with $i = 3, \dots, 6$) of the four jets, the cosines of the opening angles between partons ($\cos \omega_{ij}$, with $i, j = 3, \dots, 6$ and $i \neq j$), and the scaled masses ($\mu_{ij} = m_{ij}/\sqrt{s}$, with $i, j = 3, \dots, 6$ and $i \neq j$) of parton pairs. In addition, three variables characterizing the orientation of event planes are investigated. One of the three variables is the Bengtsson-Zerwas angle (χ_{BZ}) [?] defined (Figure 4) as the angle between the plane containing the two leading jets and the plane containing the two non-leading jets:

$$\cos \chi_{BZ} = \frac{(\vec{p}_3 \times \vec{p}_4) \cdot (\vec{p}_5 \times \vec{p}_6)}{|\vec{p}_3 \times \vec{p}_4| |\vec{p}_5 \times \vec{p}_6|}$$

The second variable is the cosine of the Nachtmann-Reiter angle [?] ($\cos \theta_{NR}$) defined as the angle between the momentum vector differences of the two leading jets and the two non-leading jets:

$$\cos \theta_{NR} = \frac{(\vec{p}_3 - \vec{p}_4) \cdot (\vec{p}_5 - \vec{p}_6)}{|\vec{p}_3 - \vec{p}_4| |\vec{p}_5 - \vec{p}_6|}$$

Figure 4 illustrates the definitions of χ_{BZ} and θ_{NR} variables. Historically, χ_{BZ} and θ_{NR} were proposed for e^+e^- collisions to study gluon self-coupling. Their interpretation in pp collisions is more complicated, but the variables can be used as a tool for studying the internal structure of the four-jet events.

The variables proposed by Korner, Schierholz and Willrodt, ϕ_{KSW} , [?] is defined for events for which there are two jets in both hemispheres defined by the thrust axis. ϕ_{KSW} is the angle between the normals to the plane containing the jets in one hemisphere and to the plane defined by the other two jets. Gluon alignment in the splitting process $g \rightarrow gg$ favours $\phi_{KSW} \sim \pi$, whereas $g \rightarrow q\bar{q}$ prefers the planes to be orthogonal.

3 Monte Carlo Sample and Event Selection

The MC sample used for this analysis consists of simulated QCD dijet events at $\sqrt{s} = 10$ TeV pp collisions. They are produced in the context of the Summer08 official CMS production with the PYTHIA 6.416 [?] event generator using the DWT tune [?] in 21 \hat{p}_T bins. The PYTHIA event generation is based on leading order (LO) matrix elements of $2 \rightarrow 2$ processes matched with a parton shower to describe multi-jet emission due to initial and final state radiation. In the analysis we make use of the QCD multi-jet events consisting of the Standard Model process $qq \rightarrow qq$, $gq \rightarrow gq$, $qq \rightarrow gg$, $gg \rightarrow qq$ and $gg \rightarrow gg$ (where q stands for a quark and g for a gluon) within the range $0 < \hat{p}_T < 5000$ GeV/c, where \hat{p}_T is defined as the momentum of the exchanged parton in the LO matrix element. The events have been passed through a full GEANT4 [?] based simulation of the CMS detector. The generation is done in the CMS software version 2_1_7 and the reconstruction using 2_1_8 assuming the IDEAL V9 detector conditions. It should be noted that there are two important new features in this version of the CMS software which will affect the relative jet response: first the HF calorimeter response to jets has been lowered by a constant factor of 0.7 and second the HO energy is not used for the reconstruction of the jet p_T . The exact string defining the samples in DBS is /QCDDiJetPt*to*/Summer08 IDEAL V9 v*/GEN-SIM-RECO. The phase space range of each sample as well as the corresponding cross-section and the number of events used, are summarized in Table 2.

Sample	\hat{p}_T (GeV)	σ (pb)	Events processed
QCDDiJetPt0To15	0-15	5.156e10	101054
QCDDiJetPt15To20	15-20	9.494e8	142560
QCDDiJetPt20To30	20-30	4.010e8	87300
QCDDiJetPt30To50	30-50	9.47e7	136800
QCDDiJetPt50To80	50-80	1.22e7	103545
QCDDiJetPt80To120	80-120	1.617e6	51300
QCDDiJetPt120To170	120-170	2.56e5	50085
QCDDiJetPt170To230	170-230	4.83e4	51840
QCDDiJetPt230To300	230-300	1.06e4	54000
QCDDiJetPt300To380	300-380	2.63e3	60048
QCDDiJetPt380To470	380-470	7.22e2	51840
QCDDiJetPt470To600	470-600	2.409e2	27648
QCDDiJetPt600To800	600-800	62.492	28620
QCDDiJetPt800To1000	800-1000	9.421	20880
QCDDiJetPt1000To1400	1000-1400	2.343	24640
QCDDiJetPt1400To1800	1400-1800	1.568e-1	27744
QCDDiJetPt1800To2200	1800-2200	1.38e-2	22848
QCDDiJetPt2200To2600	2200-2600	1.296e-3	22560
QCDDiJetPt2600To3000	2600-3000	1.14e-4	22800
QCDDiJetPt3000To3500	3000-3500	8.43e-6	20880
QCDDiJetPt3500Toinf	> 3500	1.81e-8	34320

Table 1: Details of the MC samples used in the present analysis.

The distributions are obtained by summing the distribution from each bin with appropriate weight ($wt = \frac{\sigma}{N}$ where σ and N are cross section and number of generated events for the \hat{p}_T bin). The combined distribution is then scaled to give an integrated luminosity of 10 pb^{-1} .

We use SisCone algorithm [4] for jet reconstruction in this analysis. SisCone is both infrared and collinear safe and does not leave unclustered energy, and is preferred by theorists over traditional cone based clustering algorithm. SisCone has been fully integrated into CMS software framework and is adopted as the default cone based algorithm for CMS. Events are preselected by requiring at least two calorimeter jets with raw (uncorrected) transverse energy $E_T > 30 \text{ GeV}$ within a region of $|\eta| < 3.0$ (within the endcap region of the CMS calorimeter) which we consider specially suitable for early data analysis. Events are selected by demanding the leading jet to be above p_T threshold of 110 GeV . Inclusive 3- or 4-jet events are selected where each jet has above 50 GeV .

4 Trigger selection

The jet clustering algorithm used at the trigger level is the SisCone algorithm (with radius $R = 0.5$). Table 2 summarizes the transverse energy thresholds and the expected prescale factors for the various triggers. The expected prescale factors are given for two different luminosity conditions ($\mathcal{L} = 8 \cdot 10^{29} \text{ cm}^{-2}\text{s}^{-1}$).

Sample	HLT15	HLT30	HLT50	HLT80	HLT110
MC prescale	25×40	25×1	1×5	1	1

Table 2: Trigger table proposed for $\mathcal{L} = 8 \cdot 10^{29} \text{ cm}^{-2}\text{s}^{-1}$.

We chose to perform the analysis with single jet trigger as it will provide enough data for our measurement. We choose our events based on HLT80 as a single jet trigger and decided the offline thresholds accordingly where we have more than 99% efficiency.

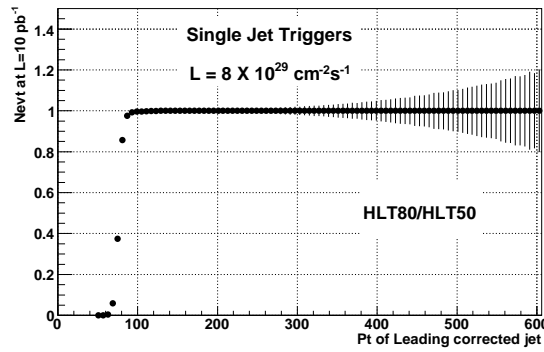


Figure 5: Efficiency of the single jet trigger used in the analysis.

5 Multi-jet topological distributions

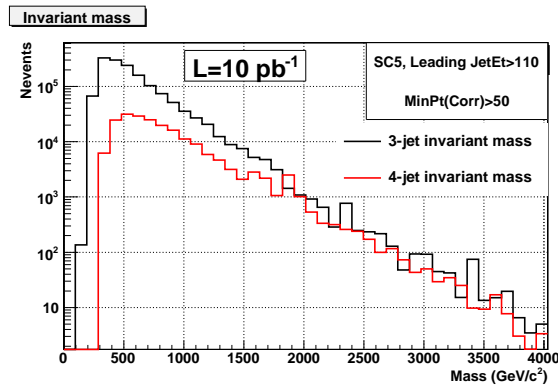


Figure 6: Distribution of invariant mass of the 3- and 4-jet events as expected from integrated luminosity of 10 pb^{-1} .

After the primary event selection three jet events are selected by further demanding that there be at least three jets. The separation ΔR between jets is required to be greater than twice the cone size ($\Delta R = 1$ for SisCone 5 for example), to avoid systematic uncertainty associated with the merging or splitting of the cone jet algorithm. This requirement removes events with overlapping jets and therefore ensures good jet energy and direction measurements.

The surviving events are then transformed to the CM frame of the three leading jets. Any other jets in the event are ignored. The jets are reordered in descending energy in their CM system. The topological variables (x_3 , x_4 , $\cos \theta_3$ and ψ) are calculated.

Four jet events are selected in similar manner. Events are required to have at least four jets. The four leading jets are boosted to their centre of mass frame and are ordered in decreasing energy.

The invariant mass distribution of the three(four) highest p_T jets in case of 3(4)-jet events is shown in Figure 6.

5.1 Topologies of Three-Jet events

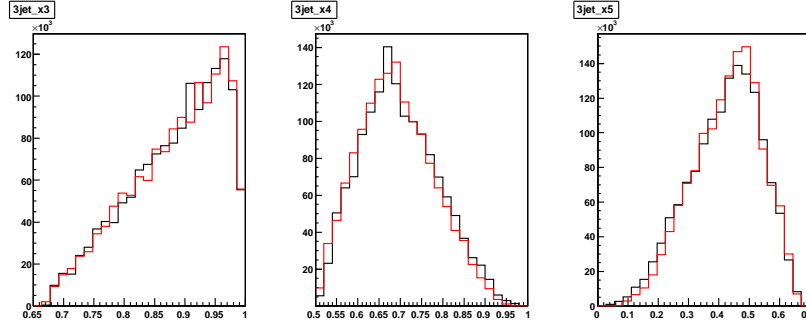


Figure 7: Distribution of energy fractions of the three jets at $\sqrt{s} = 10$ TeV with integrated luminosity of 10 pb^{-1} . In each plot the red line corresponds to the corrected calorimetric jet and the black line corresponds to the generator level jets.

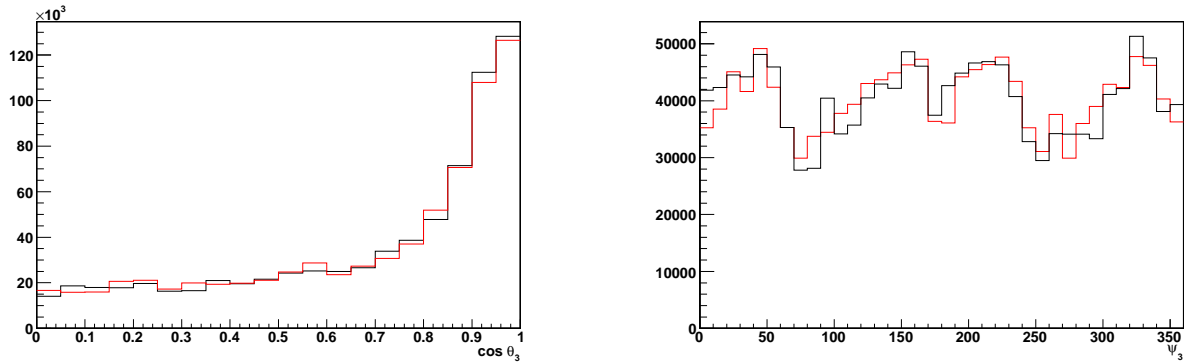


Figure 8: The three jet topological distributions. In each plot the red line corresponds to the corrected calorimetric jet and black line corresponds to the generator level jets. Left is the plot of Cosine of the polar angle of the hardest jet with respect to the beam ($\cos \theta_3$). Right is the plot of The angle between the plane containing partons 1 and 3 and the plane containing partons 4 and 5 (ψ).

Figures 7 and 8 show the three jet topological distributions. In Figure 7 the jet fractional energy functions (x_3 , x_4 , x_5) are presented. The three jets are labelled in order of decreasing energy in the CM frame. The average values of x_3 , x_4 and x_5 are 0.90, 0.70, 0.39 respectively. The energy distributions show a peak around 0.95 for x_3 while the peak position is shifted to 0.70 for x_4 and to 0.45 for x_5 . This is characteristic of gluon radiation.

The $\cos \theta_3$ distribution is shown in the left plot of Figure 8. As in the angular distributions of two-jet events, an angular dependence characteristic of Rutherford t-channel scattering is noticed. The large angular coverage of CMS calorimeter allows to cover the entire $\cos \theta_3$ range. The measured ψ distribution is shown in right hand side plot of Fig. 8.

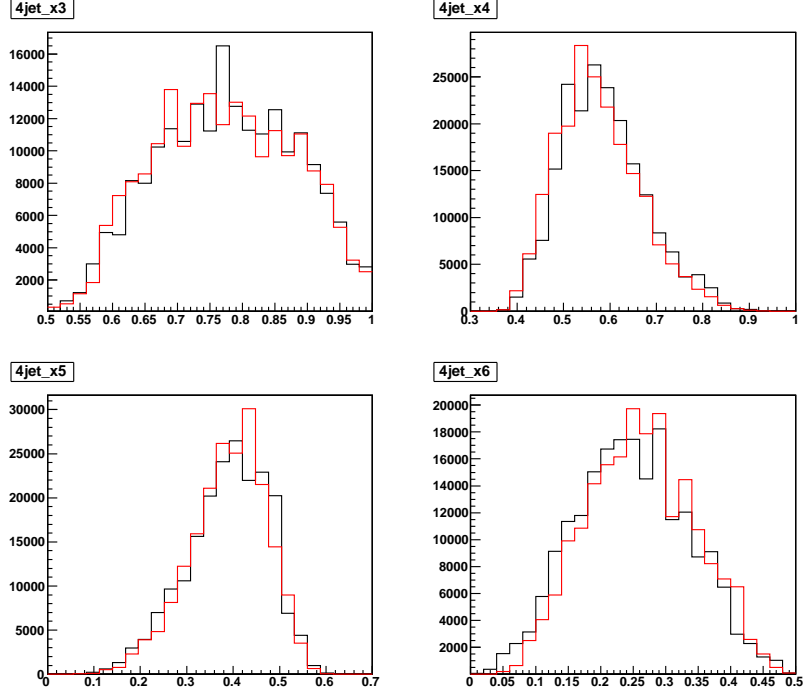


Figure 9: Distribution of energy fractions of the four jets at $\sqrt{s} = 10$ TeV with integrated luminosity of 10 pb^{-1} . In each plot the red line corresponds to the corrected calorimetric jet and black line corresponds to the generator level jets.

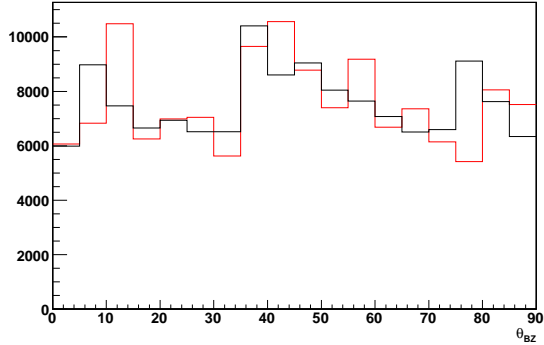


Figure 10: Angle between the plane containing the two leading jets and the plane containing the two non-leading jets (The Bengston-Zerwas angle (θ_{BZ})). The red line corresponds to the corrected calorimetric jet and black line corresponds to the generator level jets.

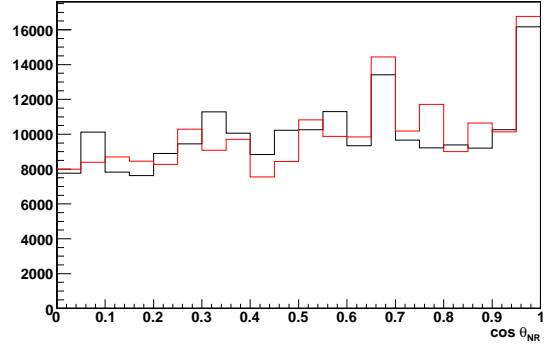


Figure 11: Angle between the momentum vector differences of the two leading jets and the two non-leading jets (the Nachtmann-Reiter angle ($\cos \theta_{NR}$)). The red line corresponds to the corrected calorimetric jet and black line corresponds to the generator level jets.

5.2 Topologies of Four-Jet events

The four measured energy fractions of four jet events are shown in Figure 9. The four jets are ordered in decreasing energy in their centre-of-mass system. Out of the four scaled energy variables shown, only three distributions are independent. The other is fixed by the condition $\sum_i x_i = 2$. The mean values for four energy fractions for corrected jets are 0.78, 0.59, 0.38 and 0.25.

Figures 10 and 11 show the measured Bengston-Zerwas and Nachtmann-Reiter angles. The Nachtmann Reiter angle is plotted as a function of cosine of the angle whereas the Bengston-Zerwas angle is plotted in unit of degrees. One sees no significant behaviour for the Bengston-Zerwas angle. Had it been a $2 \rightarrow 2$ event the distribution would have been more populated near 0 but the presence of at least 4 jets (as we assume an inclusive 4-jet process to start with) we have deviation away from 0 for the angular distribution. For the Nachtmann-Reiter angle we observe more population near 1. This may be because the sample is primarily a dijet sample. So two non-leading jets are

very less energetic compared to the two leading ones.

6 Sensitivity study

Here we check the influence of different jet clustering algorithm on the shape of the multi-jet distributions. We study the sensitivity of the multi-jet variables to the choice of jet clustering algorithm and to the effect of jet energy correction.

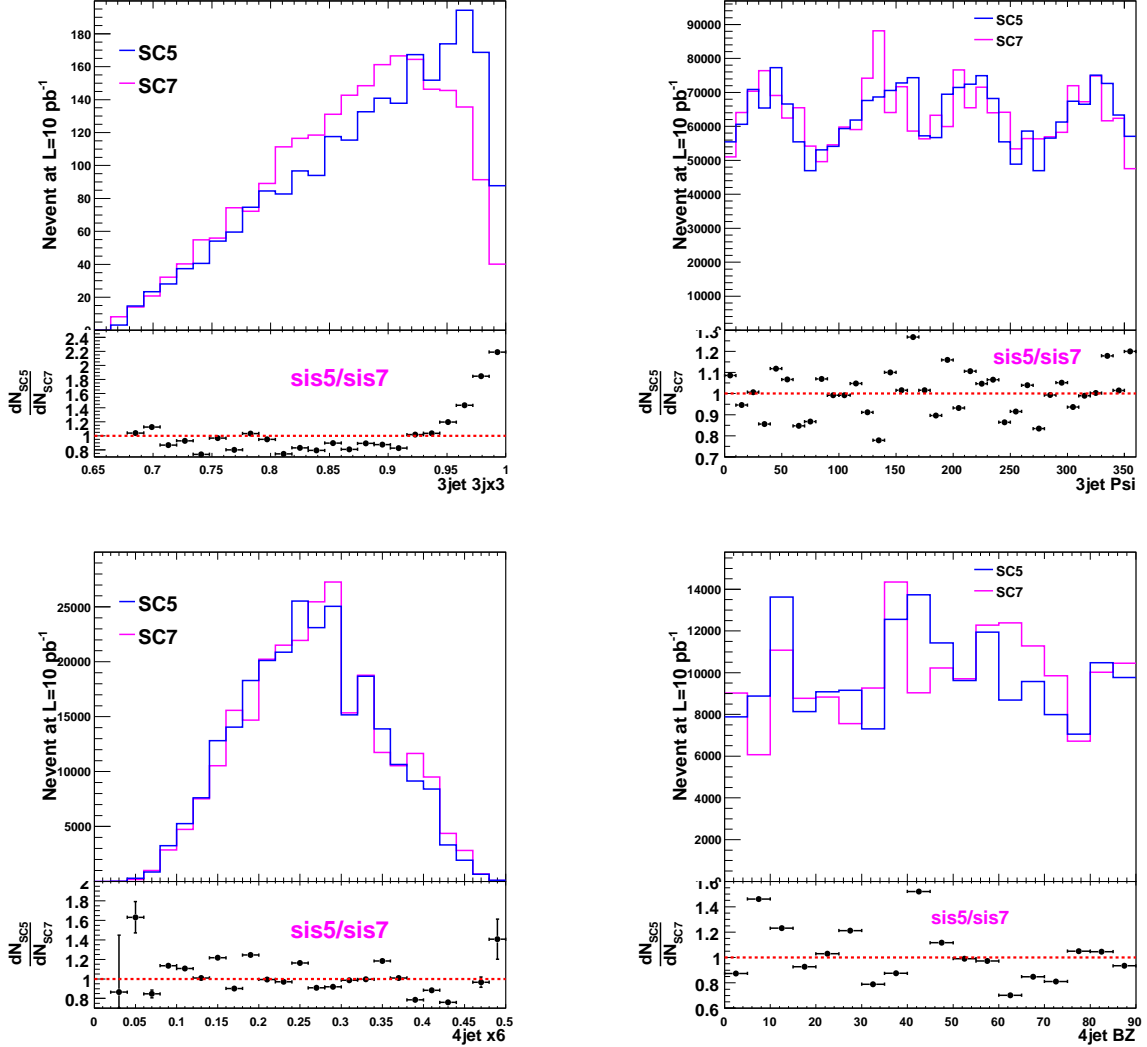


Figure 12: Distribution of multi-jet distributions under variation of the jet algorithm with isolation criteria ($\Delta R > 1.0$ for SisCone5 and $\Delta R > 1.4$ for SisCone7). The lower histogram in each figure is the ratio of distributions obtained using SisCone5 to that with SisCone7. The top left shows the hardest jet energy fraction in 3-jet case. The top right plot shows the ψ angle in 3-jet case. Bottom left plot shows the energy fraction of the 4th leading jet in 4-jet case. The Bengtson-Zerwas angle is shown in bottom right plot.

6.1 Sensitivity to jet clustering algorithms

We compare the normalized multi-jet distributions determined from jet four-vectors found with the following two jet algorithms.

- the seedless infrared safe cone algorithm with radius $R = 0.5$ (SisCone5) and an energy-sharing fraction of $f = 0.75$.

- the seedless infrared safe cone algorithm with radius $R = 0.7$ (SisCone7) and an energy-sharing fraction of $f = 0.75$.

Figure 12 shows some of the multi-jet variables for two different jet algorithms - SisCone5 and SisCone7. We notice that the distributions depend on the cone size of the algorithm. The ratio plots shown in the bottom of each plot gives a quantitative idea. The differences could be 10-20% depending on the variable.

6.2 Sensitivity due to jet energy corrections

The non-compensating and non-linear behaviour of the CMS calorimeter system is taken into account by the jet energy corrections. The correction factors are obtained using a factorized approach by applying in a first step corrections which flatten the jet energy distributions as a function of pseudo-rapidity η , using the barrel region of $|\eta| < 1.3$ as the normalization region. In a subsequent step, the calorimeter jet energies are corrected back to particle level. The corrections for the eta-dependence will be evaluated from data using dijet-balance in QCD-events and the absolute response corrections will be determined using γ/Z -jet events. The correction factors used in this analysis are based on Monte Carlo simulations in a scenario where 10 pb^{-1} of integrated luminosity has been assumed for their determination. The effect of the jet energy correction on the normalized event-shape distributions can be judged by comparing the corrected and uncorrected distributions with the corresponding generator level distribution.

Figures 7, 8, 9, 10 and 11 show that the distributions corresponding to the corrected calorimetry jet match the distributions with generated jets within 10 percent given statistical fluctuations. This will be discussed more in the next section.

7 Detector Effects

7.1 Energy resolution

The effect of the jet energy resolution is studied by applying a jet energy resolution smearing function on generator level jets and comparing these to the unsmeared jets. After the smearing, the jets are reordered in p_T . The following resolution smearing functions, which are obtained using the asymmetry method for SisCone7-jets in the barrel region as demonstrated in eq.1, has been used:

$$\frac{\sigma(p_T)}{p_T} = \sqrt{\left(\frac{6.0}{p_T[\text{GeV}/c]}\right)^2 + \left(\frac{1.4}{\sqrt{p_T[\text{GeV}/c]}}\right)^2 + (0.043)^2} \quad (1)$$

For the end cap region we use the following parameters:

$$\frac{\sigma(p_T)}{p_T} = \sqrt{\left(\frac{6.6}{p_T[\text{GeV}/c]}\right)^2 + \left(\frac{1.1}{\sqrt{p_T[\text{GeV}/c]}}\right)^2 + (0.044)^2} \quad (2)$$

7.2 Position resolution

To study the effect of position resolution we look at the effect of smearing of the angular variable (η) and the azimuthal angle (ϕ).

7.2.1 Resolution in Eta

We also study the effect of the η resolution by applying a resolution smearing function on generator jets and comparing these to the unsmeared jets. The smearing function for η in barrel region :

$$\sigma\eta = \sqrt{\left(\frac{1.31}{p_T[\text{GeV}/c]}\right)^2 + \left(\frac{0.25}{\sqrt{p_T[\text{GeV}/c]}}\right)^2 + (0.026)^2} \quad (3)$$

for endcap ($1.4 < |\eta| < 3.0$ region the function is:

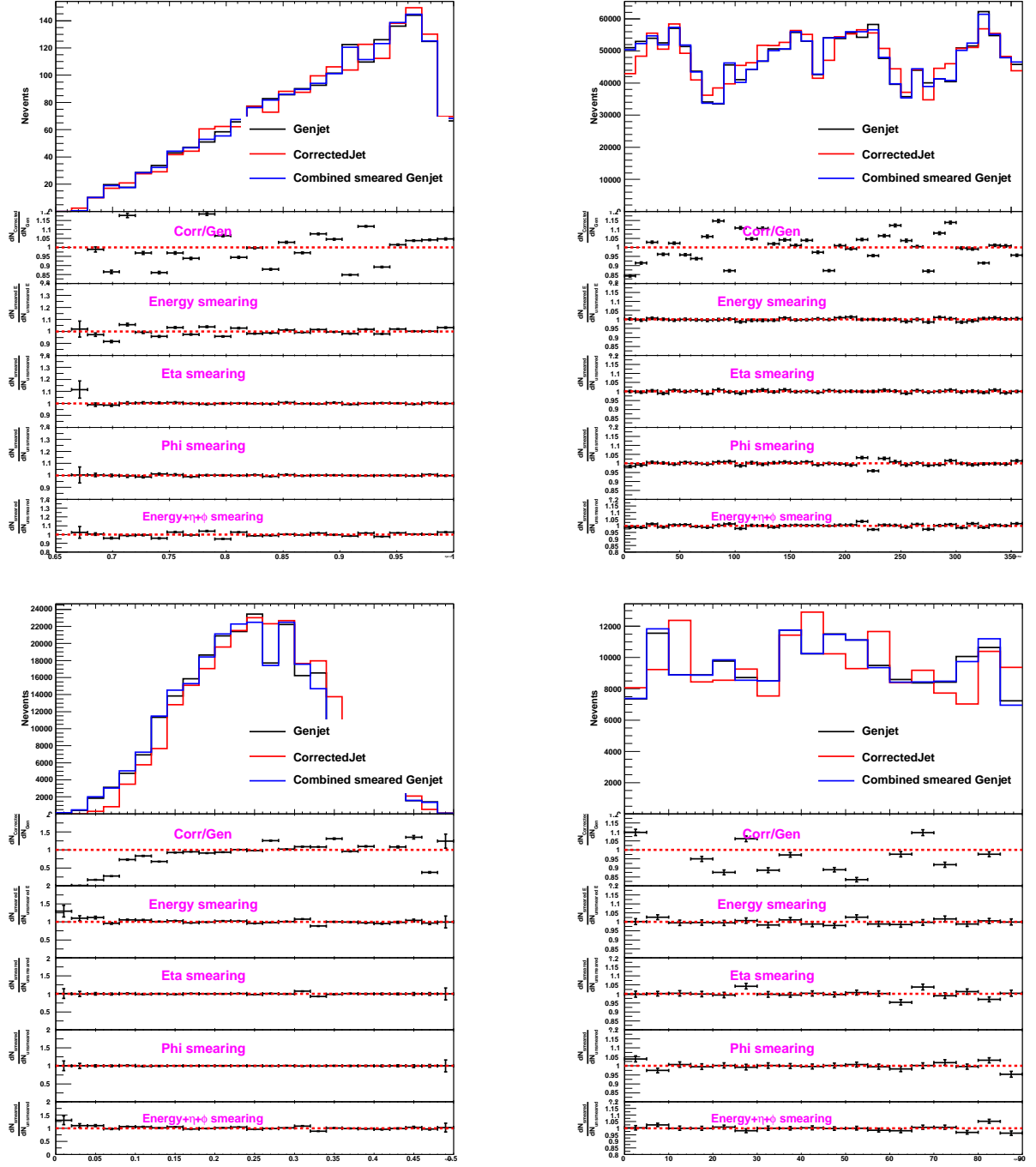


Figure 13: The effect of detector effects on the multi-jet distributions. The top left shows the hardest jet energy fraction in 3-jet case. The top right plot shows the ψ angle in 3-jet case. Bottom left plot shows the energy fraction of the 4th leading jet in 4-jet case. The Bengston-Zerwas angle is shown in bottom right plot. In each of the figure the histograms from top to bottom are as follows: distributions with genjets, corrected jets and combined smeared genjets; ratio of corrected calojets to genjets; ratio of smeared and unsmeared genjets with only energy smearing; ratio of smeared and unsmeared genjets with only eta smearing; ratio of smeared and unsmeared genjets with only phi smearing; ratio of smeared and unsmeared genjets with only energy+eta+phi smearing.

$$\sigma_{\eta} = \sqrt{\left(\frac{1.42}{p_T[\text{GeV}/c]}\right)^2 + \left(\frac{0.21}{\sqrt{p_T[\text{GeV}/c]}}\right)^2 + (0.017)^2} \quad (4)$$

for forward ($3.0 < |\eta| < 5.0$) region the function is:

$$\sigma_\eta = \sqrt{\left(\frac{1.25}{p_T[GeV/c]}\right)^2 + (0.025)^2} \quad (5)$$

7.2.2 Resolution in Phi

To study the effect of the ϕ resolution by applying a resolution smearing function on generator jets and comparing these to the unsmeared jets. The smearing function for ϕ in barrel region :

$$\sigma_\phi = \sqrt{\left(\frac{2.72}{p_T[GeV/c]}\right)^2 + \left(\frac{0.23}{\sqrt{p_T[GeV/c]}}\right)^2 + (0.004)^2} \quad (6)$$

7.3 Combined effect

After the studies of the individual effect of energy, eta and phi resolutions we proceeded to see their combined smearing effect. It is worthwhile to see whether a simple Gaussian smearing of energy, eta, phi of the jets can reproduce the detector effects as observed in the calorimeter jets after corrections. In Figure 13 the top left plot shows the energy fraction of the most energetic jet in 3-jet case. The top right plot shows the ψ angle in the 3-jet case. Bottom left plot shows the energy fraction of the 4th leading jet in the 4-jet case. The Bengston-Zerwas angle is shown as the bottom right plot. In each of these figures the histograms from top to bottom are as follows: distributions with generator level jets, corrected jets and combined smeared genjets; ratio of corrected calojets to genjets; ratio of smeared and unsmeared genjets with only energy smearing; ratio of smeared and unsmeared genjets with only eta smearing; ratio of smeared and unsmeared genjets with only phi smearing; ratio of smeared and unsmeared genjets with only energy+eta+phi smearing.

Looking at the figures 13 we see that the effect of energy smearing is marginal in scaled energy variables but almost negligible in angular variables. The effect of eta and phi smearing alone is very small for kinematic variables but more significant in angular variables. We also observe that the combined smearing fails to reproduce the overall detector effects.

8 Systematic uncertainty

The main sources of systematic uncertainties include:

- jet energy scale,
- trigger bias,
- event selection.

8.1 Jet Energy Scale

Often, the leading source of systematic errors in QCD data analysis is the limited knowledge of the jet energy scale (JES). The JES uncertainty at start up will be $\pm 10\%$. Changing the JES correction within its uncertainty changes the jet shapes as jets migrate between p_T bins. Jet shapes vary slowly with jet p_T and this effect is expected to be small. To determine the impact on the jet shapes, we changed the p_T of the jets by $\pm 10\%$ and repeated the whole analysis. We compare the ratio. From Figure 14 we see that the distributions are almost insensitive to jet energy scale corrections.

8.2 Systematic uncertainty due to trigger bias

As we took a specific trigger biased sample for our study we are interested to see the effect of the trigger bias. So we have chosen another trigger bit which is just lower to the one we were using and plotted the distributions. Figure 15 reinforces the fact that our offline event selection was indeed efficient and the choice of HLT50 instead of HLT80 does not affect the multi-jet event shape distributions. There is no significant trigger bias in these variables.

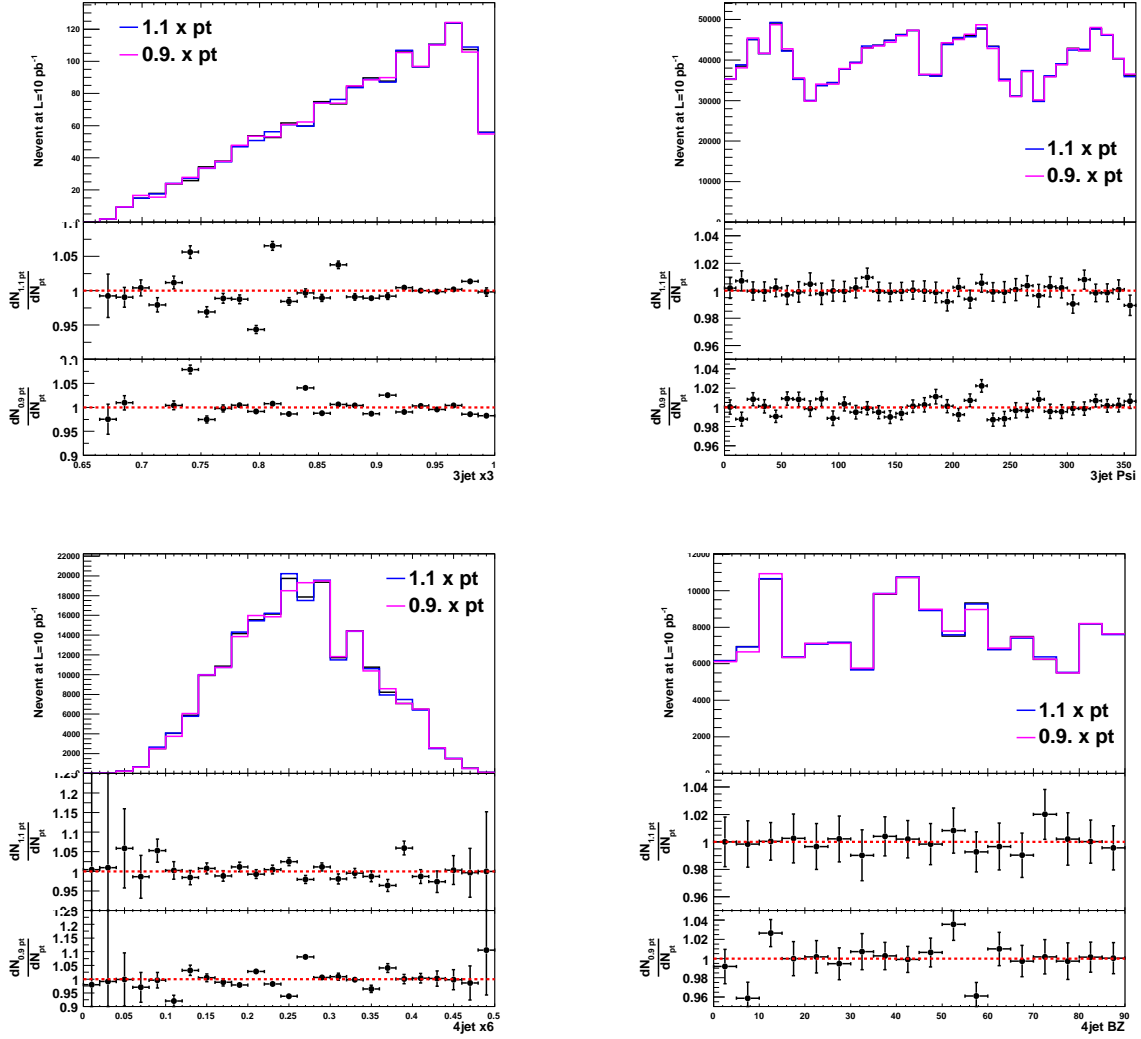


Figure 14: The effect of jet energy scale on the multi-jet distributions. The top left shows the energy fraction of the hardest jet in the 3-jet case. The top right plot shows the ψ angle in 3-jet case. Bottom left plot shows the energy fraction of the 4th leading jet in the 4-jet case. The Bengston-Zerwas angle is shown in bottom right plot.

8.3 Systematic uncertainty due to event selection

We put an offline cut on the leading jet p_T of the chosen HLT trigger sample. We also demanded all the jets to have p_T greater than a certain minimum threshold. We would like to see how robust our event selection is by varying the thresholds on the leading jet p_T by 10%.

Fig. 16 shows the effect of event selection criteria. We observe that by relaxing the event selection criteria the scaled energies deviate by less than 10% whereas the variable ψ deviate within 5% and the Bengston-Zerwas angle (θ_{BZ}) deviate within 5% which is well within the statistical fluctuations.

Thus the leading jet threshold put some systematic effect on the distributions.

9 Comparison to matrix element calculations

In order to demonstrate the sensitivity of hadronic multi-jet distributions to different models of multi-jet production, we compare the distributions, as we expect them to be measured based on an integrated luminosity of 10 pb^{-1} , to the generator level predictions as obtained from two generators that contain different models of QCD multi-jet production, PYTHIA 6.409 and ALPGEN 2.12 [?]. PYTHIA is based on a leading-order matrix elements of $2 \rightarrow 2$ processes complemented by a parton shower while ALPGEN uses matrix element calculation.

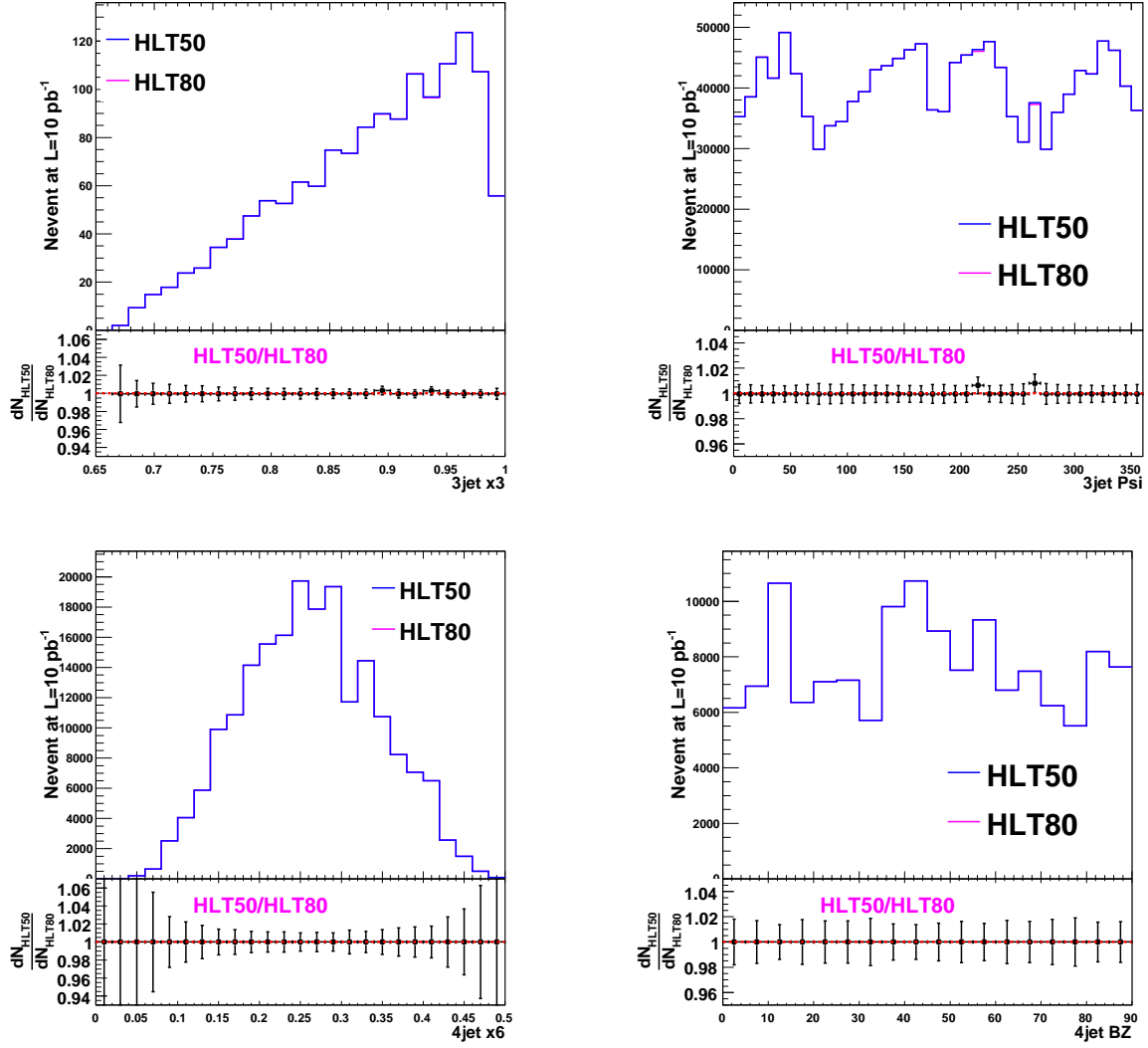


Figure 15: The effect of trigger bias on the multi-jet distributions. The top left shows the energy fraction of the most energetic jet in the 3-jet case. The top right plot shows the ψ angle in the 3-jet case. Bottom left plot shows the energy fraction of the 4th leading jet in the 4-jet case. The Bengston-Zerwas angle is shown in bottom right plot.

9.1 ALPGEN production

In ALPGEN, QCD multi-jet events are produced by calculating the multi-leg matrix elements at tree-level which are then passed to PYTHIA for the parton shower and hadronization. The ALPGEN samples used in our study contain QCD processes from 2 up to 6 jets with a minimum jet $p_T > 20$ GeV/c, using a jet matching cone of $\Delta R_{\min} = 0.7$. All other parameters are left to their default values. Using these parameter choices, some distinct differences between the PYTHIA and ALPGEN samples can be noted. In ALPGEN the jet multiplicities is found to be larger than in PYTHIA, because of more precise multi-leg matrix element treatment. Transverse energy spectra of the four hardest jets are in good agreement between both the generators.

9.2 Comparison to ALPGEN

Fig. 17 shows that there is significance difference among the distributions for PYTHIA and ALPGEN reflecting the difference underlying matrix element calculations and the different parameter choices. The results show that the multi-jet variables can be powerful handles in comparing and tuning different models of multi-jet production.

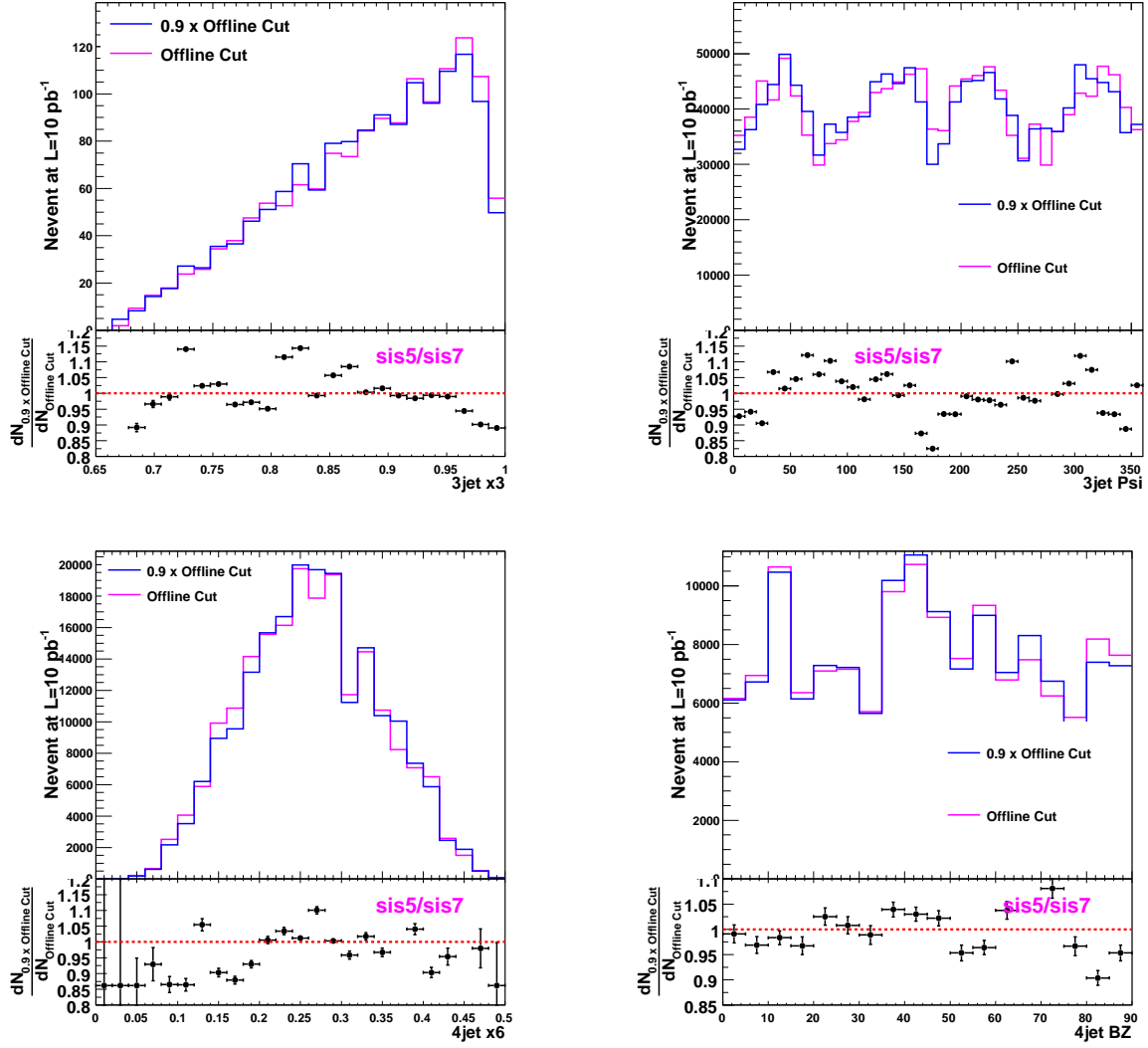


Figure 16: The effect of event selection on the multi-jet distributions. The top left shows the energy fraction of the most energetic jet in the 3-jet case. The top right plot shows the ψ angle in the 3-jet case. Bottom left plot shows the energy fraction of the 4th leading jet in the 4-jet case. The Bengston-Zerwas angle is shown in bottom right plot.

10 Conclusions

In this note we demonstrate the use of multi-jet variables at the LHC. The variables are evaluated using calorimeter jet momenta with corrections as input. They are shown to have some dependence to jet algorithms used and dependent on the effect of jet energy corrections. We present an estimate of the dominant systematic uncertainties at the start up, resulting from jet energy resolution effects and from limited knowledge of jet energy scale. Using examples of kinematic variables - scaled energy of the hardest and softest jets and also the angle between jet planes, we show that early measurements of multi-jet variables allow us to study the difference in modelling of QCD multi-jet production.

References

- [1] S. Abachi et al., “*Studies of topological distributions of inclusive three and four jet events in $\bar{p}p$ collisions at $\sqrt{s} = 1800\text{GeV}$ with the D0 detector.*”, Phys. Rev. D, **53**, No. 11 (1996) and the references therein.
- [2] B. Adeva et al, *A test of QCD based on 3-jet events from Z^0 decays.*, Physics Letters B, **263**, No.3,4 (1991)
- [3] B. Adeva et al, *A test of QCD based on 4-jet events from Z^0 decays.*, Physics Letters B, **248**, No.1,2 (1990)
- [4] P. Schieferdecker et al., “*Performance of the SIScone Jet Clustering Algorithm.*” CMS AN-2008/002.

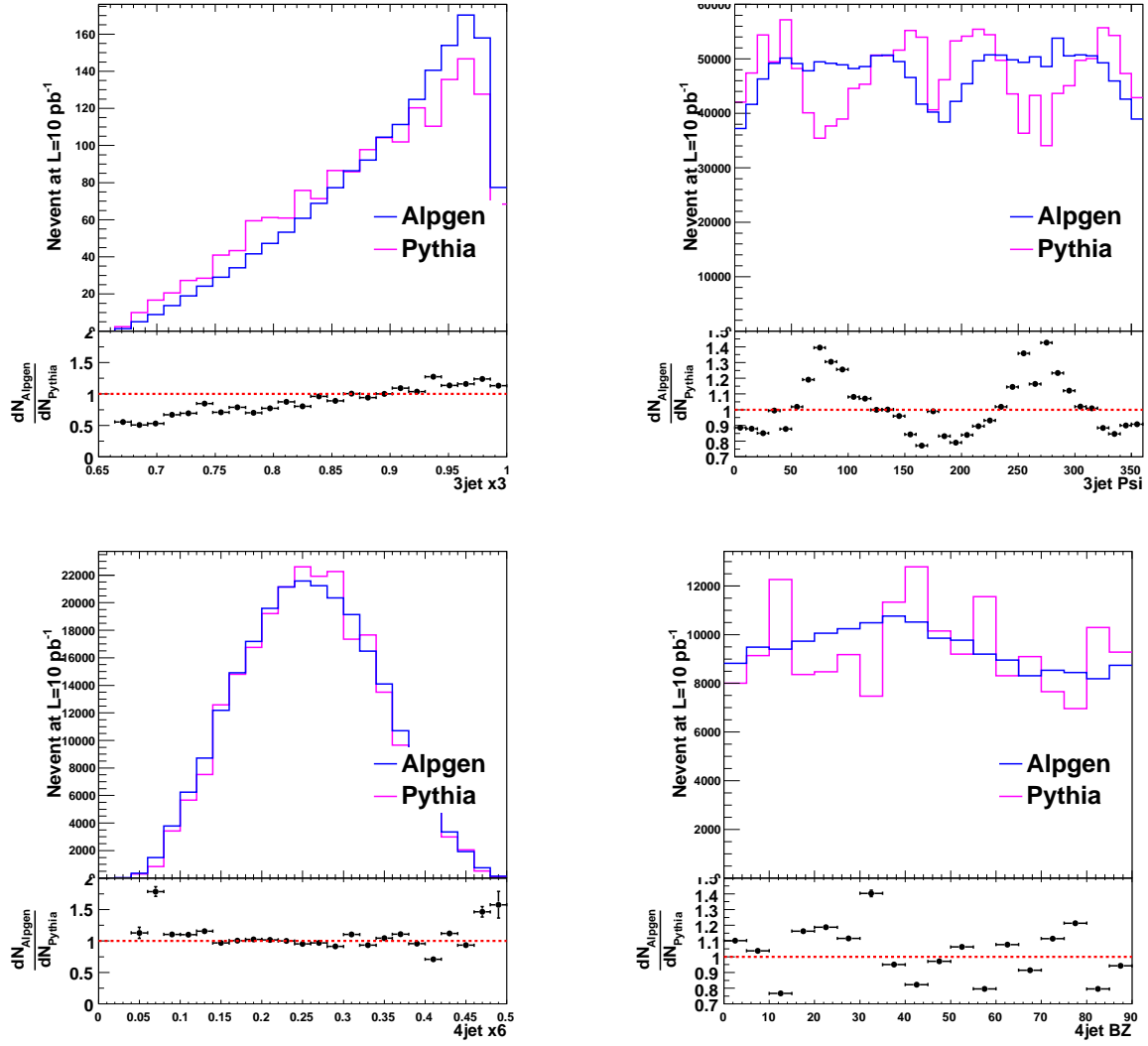


Figure 17: Multi jet distributions for PYTHIA and ALPGEN. The top left shows the energy fraction of the most energetic jet in the 3-jet case. The top right plot shows the ψ angle in the 3-jet case. Bottom left plot shows the energy fraction of the 4th leading jet in the 4-jet case. The Bengtson-Zerwas angle is shown in bottom right plot.